Enhanced CO Detection Using Potentiometric Sensors Based on PIM1/DBU Imidazolate Membranes

ADVANCED SUSTAINABLE SYSTEMS
www.advsustainsys.com

Enhanced CO_2 Detection Using Potentiometric Sensors Based on PIM-1/DBU Imidazolate Membranes

Davide Molino, Giuseppe Ferraro, Stefania Lettieri, Pietro Zaccagnini, Marco Etzi, Carmela Astorino, Eugenio De Nardo, Mattia Bartoli, Andrea Lamberti, Candido Fabrizio Pirri, and Sergio Bocchini**

A novel potentiometric sensor for carbon dioxide (CO_2) detection utilizing a composite membrane of Polymer of Intrinsic Microporosity (PIM-1) and 18-diazabicyclo[5.4.0]undec-7-ene imidazolate (DBU-imidazolate) is presented. The high surface area and gas permeability of PIM-1, combined with the chemical affinity and ion-exchange properties of DBU-imidazolate, contribute to enhanced CO_2 sensitivity and selectivity. The research objectives included the synthesis of PIM-1 and DBU-imidazolate, the preparation of composite membranes, and the evaluation of their performance as CO_2 sensors. Solvent casting and impregnation methods are employed to prepare the membranes, which are characterized using Thermal Gravimetric Analysis (TGA), and Field Emission Scanning Electron Microscopy (FESEM). CO_2 absorption tests and Electrochemical Impedance Spectroscopy (EIS) are conducted to assess the sensors' performance. The PIM-1/DBU-imidazolate membrane exhibited high efficiency in CO_2 capture and release. Open circuit voltage (OCV) measurements are performed under varying concentrations of CO_2 exposure and cycles of adsorption/desorption. Results show that the membrane achieves steady state faster at higher CO_2 concentrations, with a logarithmic relationship between CO_2 concentration and voltage variation, indicating potential for CO_2 detection in human environments. These results confirm the sensor's ability to detect varying CO_2 concentrations, highlighting its potential for reliable and efficient CO_2 monitoring in environmental and industrial applications.

1. Introduction

Carbon dioxide (CO_2) naturally occurs in the atmosphere at levels ranging from 350 to 400 parts per million (ppm), with urban areas often experiencing higher concentrations. These levels of CO_2 are a matter of both scientific and public concern due to their impact on global warming and climate change.[1] Detecting CO_2 is essential across various applications, including monitoring indoor air quality, in the food industry, and within healthcare settings. Workplace regulations stipulate that CO_2 concentrations in workspaces should remain below 5000 ppm on an 8 h average.[2] Nevertheless, even lower concentrations can lead to discomfort, headaches, or fatigue, particularly for sensitive individuals. Elevated CO_2 levels have also been associated with decreased performance among schoolchildren.[3]

Gas sensors have found extensive applications in various fields such as detecting industrial gas leaks, monitoring indoor and outdoor air quality, determining the quality of food items and cosmetics, and aiding in medical diagnostics.[4,5] The market for gas sensing technology has witnessed significant growth in recent years, with projections indicating a potential net revenue of US$920 million by 2021.[6]

In contrast to conventional techniques such as gas chromatography, electrochemical gas sensors offer increased sensitivity, reduced costs, and lower power consumption.[7,8]

Based on their operational mechanisms, electrochemical CO_2 gas sensors can be categorized into several types including surface acoustic wave,[9,10] resistance,[11–13] optical,[14,15] quartz crystal microbalance,[16,17] potentiometric,[18–20] amperometric,[19,20] and capacitive.[21] Among these, commercially prevalent CO_2 gas sensors primarily rely on chemical resistance, detecting changes in electrical conductivity within gas sensing materials across diverse atmospheres.[22]

Potentiometric sensors stand out as the most widely used, also for CO_2 detection, being less energy consuming as they function as low-power electronic devices. Moreover, they offer

D. Molino, G. Ferraro, S. Lettieri, P. Zaccagnini, C. Astorino, E. De Nardo, A. Lamberti, C. F. Pirri, S. Bocchini
Department of Applied Science and Technology
Politecnico di Torino
Corso Duca Degli Abruzzi 24, Turin 10129, Italy
E-mail: giuseppe.ferraro@polito.it; sergio.bocchini@polito.it
D. Molino, G. Ferraro, S. Lettieri, P. Zaccagnini, M. Etzi, C. Astorino, E. De Nardo, M. Bartoli, A. Lamberti, C. F. Pirri, S. Bocchini
Center for Sustainable Future Technologies (CSFT)
Istituto Italiano di Tecnologia (IIT)
Via Livorno 60, Turin 10144, Italy

The ORCID identification number(s) for the author(s) of this article can be found under https://doi.org/10.1002/adsu.202400415

DOI: 10.1002/adsu.202400415

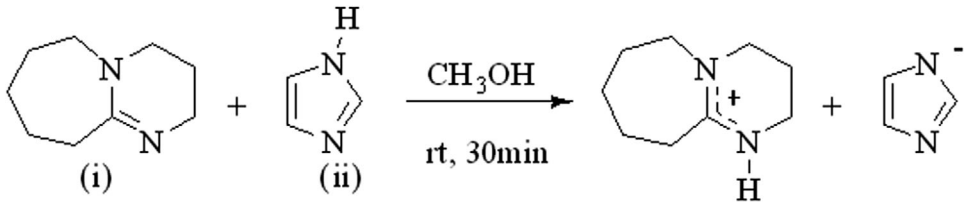

Figure 1. Synthesis of an imidazolium-based ionic liquid (IL). Equimolar amounts of 1,5-diazabicyclo[5.4.0]undec-7-ene (i) and imidazolium (ii) are mixed in methanol, followed by solvent removal and vacuum outgassing to yield the IL.

advantages such as simple operation, and a large dynamic range.[23]

They comprise two primary components: a working electrode (WE) and a reference electrode (RE). Any change in the measured potential can serve as an indicator of gas concentrations.[24] Consequently, real-time information can be obtained directly by measuring the potential difference between the two electrodes using a voltmeter.[25,26]

Polymers of intrinsic microporosity (PIMs) boast intricate networks of tiny pores, granting them exceptional gas permeability. Ionic Liquids (ILs), with their unique properties, exhibit remarkable CO_2 solubility. Combining these materials creates PIM-IL composites, a synergistic platform for not only CO_2 separation but also CO_2 sensing.

Our research group has previously explored PIM-1, a well-known PIM, alongside ILs for CO_2 separation. We exploited the ILs' ability to enhance CO_2 solubility, as demonstrated in our work.[27] However, the principle behind CO_2 separation in these composites extends beyond solubility. As CO_2 molecules diffuse into the PIM matrix, they interact with the embedded IL, altering its electrical conductivity due to the conductive nature of ILs. This change in conductivity manifests as a measurable shift in resistance, directly correlating to the CO_2 concentration within the composite.

This additional functionality paves the way for PIM-IL composites to be utilized not only for CO_2 separation but also for highly sensitive CO_2 sensing applications.

A PIM-1 membrane wetted with [DUBH][Im] results in a sensor that exhibits selective detection for CO_2 at room temperature. The reduced porosity and blocked open voids of PIM-1 induced by the presence of IL selective toward CO_2 enhances the gas selectivity in the detection process. This study demonstrates the feasibility of tuning gas-sensing properties of a PIM-1 membrane impregnated with ILs, offering new perspectives for the development of PIM-based sensors.

Moreover, in the context of gas sensing, ILs can suffer from leakage or flow-related issues when employed in "membrane-free" sensor devices. To overcome this limitation, we propose an IL-embedded membrane approach utilizing a PIM-1 polymer to prevent IL leakage. The unique properties of PIM, coupled with its symphonic effect of the polymer, contribute to a more robust and effective sensing device, addressing the issue of ILs escaping from the system. We present a comprehensive investigation into the optimization of DBU-PIM-1 membranes. Initially, we prepared the films as blended membranes and subsequently by wetting the PIM-1 membrane with IL. Next, these novel membranes were tested at various CO_2 concentrations as gas sensors, demonstrating their potential as sensing materials.

2. Experimental Section

2.1. Materials

3,3,3′,3′-Tetramethyl-1,1′-spirobiindane-5,5′,6,6′-tetraol, 1,5-Diazabiciclo (5.4.0) undec-7-ene (DBUH), Imidazolium, anhydrous K_2CO_3, methanol, Dry N,N-Dimethylformamide (DMF), and chloroform ($CHCl_3$) were purchased from Merck-Sigma-Aldrich. 2,3,5,6-Tetrafluoroterephtalonitrile was purchased from FluoroChem. All solvents and reagents were used as received without further purification.

2.2. Synthesis of PIM-1

PIM-1 was synthetized following a previously reported procedure.[28] Briefly, a mixture of anhydrous K_2CO_3 (5.53 g, 0.04 mol, FW = 138.205), 3,3,3′,3′-Tetramethyl-1,1′-spirobiindane-5,5′,6,6′-tetraol (3 g, 0.008813 mol, FW = 340.41) and 2,3,5,6-Tetrafluoroterephthalonitrile (1.76 g, 0.008813 mol, FW = 200.096) in dry DMF (60 mL) was stirred at 65 °C for 72 h under N_2 atmosphere. The crude was then poured in 400 mL of DI water and the precipitate was washed by centrifugation several times in water and methanol. After drying under vacuum overnight a bright yellow solid was obtained in a quantitative yield.

2.3. Synthesis of $[DBUH]^+[Im]^-$

Equimolar amounts of 1,5-diazabiciclo(5.4.0)undec-7-ene (36.67 g, 0.24 mol, FW = 152.24) and imidazolium (16.40 g, 0.24 mol, FW = 68.08) were mixed with 200 mL of methanol at RT under stirring for 30 min (**Figure 1**). After solubilization, the solvent was removed using a rotary evaporator. The IL was outgassed under a dynamic vacuum at 80 °C overnight until constant weight.

2.4. Membrane Preparation

2.4.1. Blended PIM-1/IL Membranes

Blended PIM-1/IL membranes were fabricated using a solvent casting method. Initially, 4 mL of $CHCl_3$ was used to dissolve PIM-1, and the solution was stirred at 40 °C for 30 min. Separately, [DBUH][Im] was dissolved in 1 mL of $CHCl_3$. The [DBUH][Im] was incorporated at two different concentrations: 25

Table 1. Membrane measured thicknesses, and corresponding densities.

Membrane	Thickness [μm]	Density [g cm^{-3}]
PIM-1	26 ± 8	0.558 ± 0.004
PIM + DBU_25 wt%	11 ± 5	1.272 ± 0.026
PIM + DBU_50 wt%	22 ± 14	1.218 ± 0.028
PIM + DBU_Imp	40 ± 10	0.814 ± 0.006

and 50 wt%. These two solutions were then combined, and additional $CHCl_3$ was added to achieve a total volume of 12 mL.

The blended solutions were cast onto a leveled aluminum substrate at room temperature. After solvent evaporation, the polymer films were formed. To facilitate self-detachment from the aluminum foil support, the membranes were immersed in a deionized water bath at room temperature. Subsequently, the membranes were blotted dry with filter paper and subjected to vacuum drying at 40 °C until a constant weight was achieved. This step ensured the complete removal of any residual solvent or water. The membranes were named respectively PIM + DBU_25 wt% and PIM + DBU_50 wt%.

2.4.2. Impregnated PIM-1 Membrane

A bare PIM-1 membrane was prepared using a solvent-casting method. PIM-1 was dissolved in $CHCl_3$ to a total concentration of 2 wt% and stirred at 40 °C for 15 min. The solution was then cast onto a leveled aluminum substrate at room temperature. The resultant membrane was dried under vacuum at 40 °C for at least 16 h to ensure the removal of any remaining solvent traces.

To impregnate the membrane, the dried PIM-1 membrane was wetted with [DBUH][Im]. The membrane underwent three cycles of vacuum and ambient pressure to facilitate thorough impregnation. Following this, the membrane was stored in [DBUH][Im] under vacuum at room temperature for 1 h. Finally, the membrane was transferred onto filter paper to remove any excess [DBUH][Im] and named PIM + DBU Imp.

2.4.3. Membrane Densities

To calculate the density of the membranes, predefined areas were cut, weighed, and their volumes were calculated based on the measured thickness. Membrane thicknesses were measured using a micrometer thickness gauge, averaging the measurements from five randomly selected points on each membrane (**Table 1**). The measured thicknesses of the membranes ranged from 11 to 40 μm. The densities of the membranes were found to be between 0.558 and 1.272 g cm^{-3}.

2.5. Physicochemical Characterization of Membranes

Thermogravimetric-coupled infrared absorption analyses (TGA-IR) were carried out in a thermogravimetric analyzer NETZSCH TG 209 F1 coupled by a transfer line heated at 230 °C with an infrared spectrometer Bruker TENSOR II equipped with an IR gas cell heated at 200 °C. The tests were performed by heating samples of ≈3 mg in alumina pans from 30 to 800 °C with a rate of 20 °K min^{-1}, under nitrogen flux of 40 mL min^{-1}. The FTIR analysis was collected in the absorbance mode in the range 4400–600 cm^{-1}. The first derivative of the weight profile (DTG) was calculated to better resolve the main thermal decomposition steps of the analyzed materials with Netzsch Proteus Analysis software.

Attenuated total reflection infrared spectroscopy (ATR-IR) was employed to characterize the membranes. Measurements were carried out on a Bruker Tensor II Fourier transform spectrophotometer. The spectra were acquired by accumulating 64 scans (64 for the background spectrum) in the range from 4000–600 cm^{-1} with a resolution of 2 cm^{-1}.

FESEM measurements were performed on a Zeis SupraTM 25 (Oberkochen, Germany). The thickness of the membranes was measured using a Digimatic indicator (IDC- 112B-5) with an accuracy of 1 μm. The thickness of the membranes recorded was an average value obtained from at least 25 different points of the membrane.

2.6. CO_2 Absorption Tests

The CO_2 absorption measurements were conducted by first exposing the sample to a nitrogen flow (20 ml min^{-1}) at 40 °C for 1 min to facilitate the release of any absorbed gas. The sample was then cooled to 25 °C and kept under a nitrogen flow for 120 min to establish the initial mass (minute 180). Maintaining the temperature at 25 °C, the gas was switched to a N_2/CO_2 mixture (12 ml min^{-1} of N_2 and 8 ml min^{-1} of CO_2) for 10 h to assess absorption, and the final mass was recorded (minute 780). After this period, the gas flow was reverted to pure nitrogen to evaluate desorption over an additional 8 h, and the mass was measured again (minute 1260).

2.7. Electrochemical Measurements

Electrochemical measurements were performed employing VMP-3 (Biologic), provided with potentiostat/galvanostat modules and frequency response analyzers to perform electrochemical impedance spectroscopy (EIS). EIS measurements were performed in the frequency range of [10^6,10^-2] Hz, ten points per decade, with a signal amplitude of 5 mV. Open circuit voltage (OCV) measurements were performed to evaluate the electrochemical cell response upon gas absorption. The voltage resolution was 1 mV. All the tests were conducted in a commercially available test cell (ECC-Air, from El Cell GmbH), where it is possible to perform electrochemical measurements while a gas stream is fed to the sample inside the cell.

3. Results and Discussion

3.1. Physico-Chemical Properties of PIM1-Based Membranes

3.1.1. Attenuated Total Reflectance (ATR)

Attenuated total reflectance (ATR) was performed on wetted and blended membranes and pure PIM-1 membrane to prove the

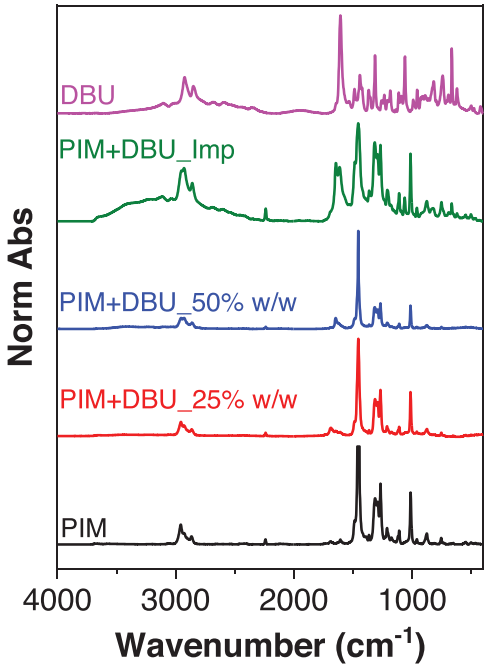

Figure 2. ATR-FTIR spectra for various samples: pure [DBUH] [Im], membranes blended with [DBUH] [Im], and impregnated membranes. pure PIM-1 membranes.

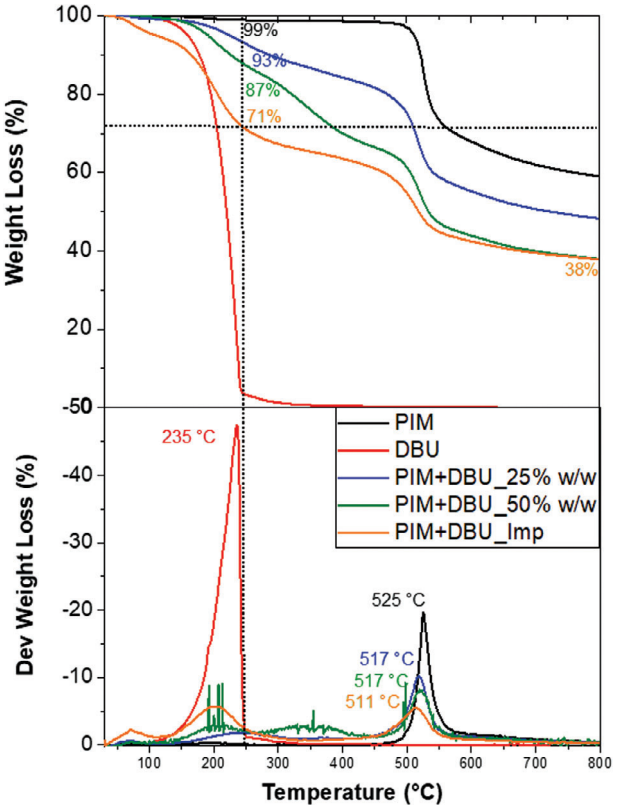

Figure 3. TGA and derivative weight loss curves of pure PIM-1 membrane, pure [DBUH][Im], composite membranes containing [DBUH][Im], and impregnated membranes containing [DBUH][Im].

successful introduction of $[DBUH]^+[Im]^-$ within the pure PIM-1 films.

In the PIM-1 membrane spectrum, the typical peaks of the polymer are present. In particular, the C-O-C stretching peak of the aromatic ethers at 1110 cm^{-1} and the CN stretching of the nitrile group at 2225 cm^{-1} are present (**Figure 2**).

The [DBUH][Im] ionic liquid exhibits characteristic signals associated with the stretching vibrations of the imidazolate aromatic ring, prominently appearing at 1580 cm^{-1}.[29] The membranes containing [DBUH][Im] exhibit distinct characteristics compared to [DBUH][Im] alone, particularly in their interaction with CO_2. The presence of CO_2 in the atmosphere and the high accessibility of ionic liquids (ILs) within the thin membrane facilitate CO_2 adsorption. This is evidenced by the appearance of a peak ≈1640 cm^{-1} in the IR spectrum, indicating the formation of carbamate groups.[30]

Furthermore, the impregnated samples show a significantly higher quantity of [DBUH][Im] compared to the membranes co-casted with [DBUH][Im]. This can be qualitatively assessed by comparing the intensity of the [DBUH][Im] bands to the PIM-1 absorption bands. The difference in band intensity highlights the more substantial presence of [DBUH][Im] in the impregnated membranes, indicating successful incorporation and retention within the membrane matrix.

3.1.2. Thermal Gravimetric Analysis (TGA)

TGA was performed on the materials to assess both the degradation pattern and thermal properties of the synthesized membranes.

In **Figure 3**, the spectra showed that the pure PIM-1 membrane underwent a single thermal degradation event at ≈525 °C (black line). As expected, the [DBUH][Im] degrade in a single step with decomposition and evaporation of the IL with a maximum degradation rate at 235 °C. In contrast, the composite membranes exhibited two distinct degradation stages: one between 200–425 °C and another between 510–520 °C, corresponding to the degradation of [DBUH][Im] and PIM-1, respectively. A minor weight loss observed below 100 °C was attributed to the loss of CO_2 absorbed from the atmosphere, corroborating previous ATR data. Additionally, the higher quantity of ionic liquid in the impregnated sample was confirmed by the greater weight loss during the initial degradation steps.

3.1.3. FESEM – Field Emission Scanning Electron Microscopy

Figure 4 highlights a comparison between mixed membranes containing DBU and pure PIM-1 membranes. Both surface topographies and cross-sections were analyzed. From the cross-sectional analysis, it is evident that increasing the amount of [DBUH][Im] in the membranes significantly alters their porosity, leading to the formation of regions rich in ionic liquid (IL) (see Figure 4f,g, before CO_2 adsorption).

After CO_2 adsorption, the PIM-1 membrane does not exhibit notable changes in morphology. In contrast, membranes

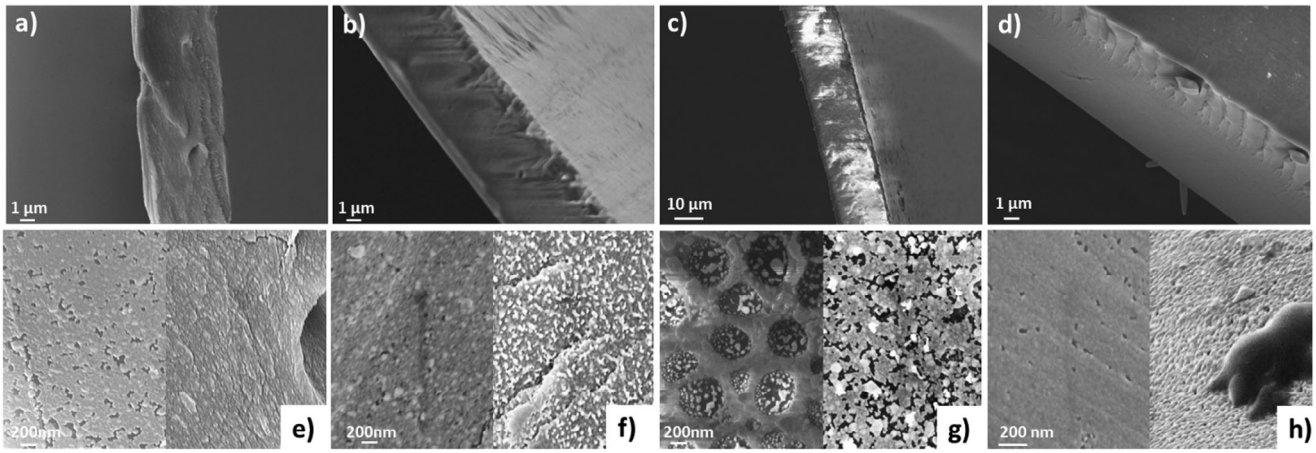

Figure 4. Cross section of. a) PIM1, b) PIM+DBU_25%, c) PIM+DBU_50%, and d) PIM_Imp membranes. Pre- (left) and post- (right) CO_2 absorption measurements of e) PIM1, f) PIM+DBU_25%, g) PIM+DBU_50%, and h) PIM_Imp membranes.

containing [DBUH][Im] show significant morphological transformations. The IL-rich regions diminish in size, forming small dark aggregates of 50 nm IM+DBU_50% while they reached of up to 350–400 µm for impregnated membranes (figure 4h). These aggregates are likely due to the formation of carbamate bonds between the ionic liquid and CO_2, resulting in the precipitation of the ionic liquid and shrinkage of the [DBUH][Im] aggregates, as previously reported for other ILs. The impregnation boosted the formation of these species reasonably due to the presence of ILs reach zone not well packed into the porous network.

3.1.4. Qualitative Evaluation of CO_2 Absorption

Figure 5 presents a qualitative assessment of CO_2 absorption as measured by TGA. The corresponding data are detailed in **Table 2**. Initially, the purging gas (N_2) was used to free the sample from water, CO_2, and other gases that may have been adsorbed prior to testing. The initial mass (column: Initial) was recorded before introducing the purging gas. Subsequently, CO_2 adsorption was conducted, and the final mass after adsorption (column: Final) was documented. Finally, the mass after desorption (column: Desorbed) was obtained following the use of the purging gas to remove the adsorbed CO_2. The pure PIM-1 membrane exhibited excellent CO_2 absorption and nearly complete desorption, with a return very close to the initial weight. This behavior highlights the efficiency of PIM-1 in reversibly capturing and releasing CO_2.

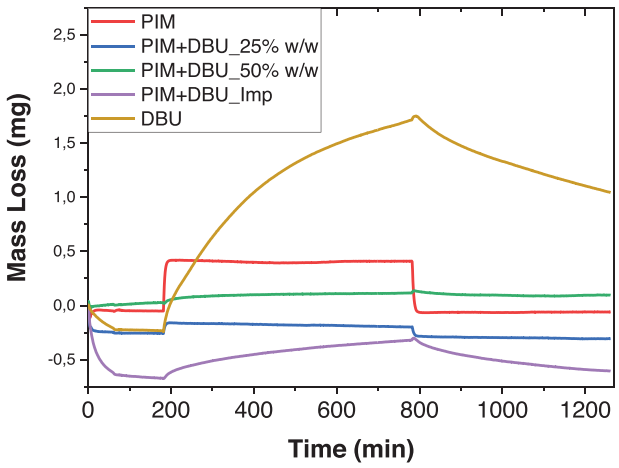

Figure 5. Qualitative CO_2 absorption and weight loss patterns across the different membrane compositions: pure PIM-1, PIM + DBU_25%, PIM + DBU_50%, PIM + DBU_Imp, and pure [DBUH]., highlighting the efficiency and reversibility of CO_2 capture for each sample.

In contrast, the PIM+DBU_25% w/w blend showed low absorption and a greater weight loss after CO_2 desorption. This is likely due to partial evaporation of the ionic liquid, which decomposes into DBU and imidazole, indicating a weak interaction between the polymer and the ionic liquid.

A similar pattern was observed for the PIM+DBU_50% blend, but in this case, a higher absorption and correspondingly lower weight loss were recorded. This suggests that a higher concentration of the ionic liquid improves CO_2 absorption while maintaining some instability.

Finally, the impregnated PIM+DBU_Imp sample demonstrated excellent absorption, as that of pure PIM-1, with better reversibility of absorption. This indicates a stronger interaction

Table 2. CO_2 absorption and desorption data for pure PIM-1, PIM + DBU_25%, PIM + DBU_50%, PIM + DBU_Imp, and pure [DBUH][Im]. Weight changes and the efficiency of CO_2 capture and release.

Sample	Mass [mg]			Abs [%]	Des [%]
	Initial min[a)]	Final[b)]	Desorbed[c)]		
PIM-1	25.87	26.34	25.87	1.78	−1.78
PIM+DBU_25%	20.70	20.75	20.65	0.28	−0.52
PIM+DBU_50%	15.81	15.90	15.88	0.57	−0.12
PIM+DBU_Imp	30.37	30.72	30.44	1.16	−0.93
DBU Pure	22.65	24.59	23.93	8.59	−2.72

[a)] Initial: Mass of the sample after being purged with N_2 to remove water, CO_2, and other adsorbed gases prior to testing. [b)] Final: Mass of the sample after CO_2 adsorption. [c)] Desorbed: Mass of the sample after the adsorbed CO_2 has been removed using the purging gas (N_2).

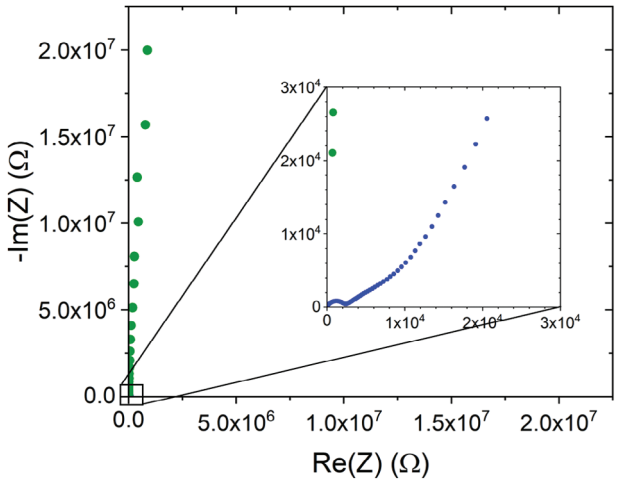

Figure 6. Comparison between EIS of blended membrane (green dots) and the one of wetted PIM (blue dots)- NYQUIST.

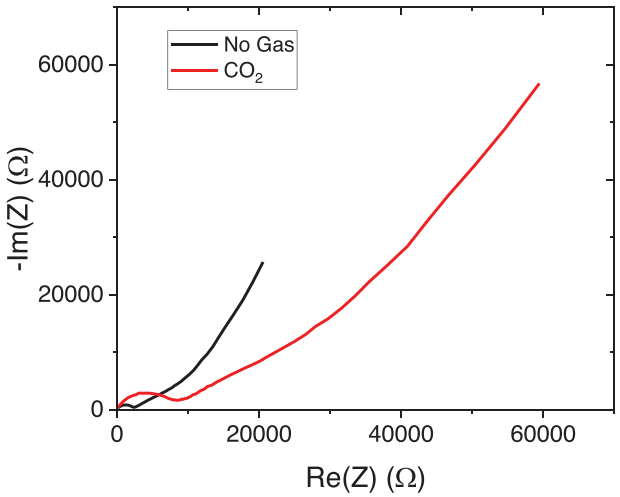

Figure 7. Comparison of Nyquist plot of wetted membrane without any gas interaction (black) and membrane post CO_2 interaction (red).

between the polymer and the ionic liquid when the latter is impregnated.

In contrast, pure [DBUH][Im] demonstrated very high CO_2 absorption, which continued to increase throughout the test without reaching a plateau, followed by minimal weight loss during desorption. This behavior is likely attributed to diffusion limitations within the ionic liquid droplet. Unlike membranes, the significant thickness of the droplet, due to surface tension and high viscosity, hampers uniform CO_2 release, resulting in slow and inefficient desorption.[31]

3.2. Electrochemical Characterization of PIM1-Based Membranes

3.2.1. EIS

The impedance of the blended and wetted PIM samples was investigated first, to probe the impedance behavior of the prepared samples. The results are reported in **Figure 6**. The blended device showed a purely capacitive behavior as can be observed from the steep increase in the Nyquist plot, corresponding to a constant phase behavior close to 90°. This behavior is typical of purely capacitive dielectric samples. The wetted PIM sample showed an electrochemical response proper of a wetted ionically conductive membrane. An overall reduced impedance module in the frequency range suggests an ionically conductive medium. The increase in the impedance module at low frequencies is due to the blocking nature of the electrodes used to probe the sample, the stainless steel of the electrochemical cell. The reported diffusive behavior might be due to the structure of the membrane, slightly impeding ionic transport.

Both samples were analyzed under CO_2 gas flow to scope eventual sensibilities to CO_2 adsorption. We found that only the wetted sample showed a remarkable impedance spectra variation both in real and imaginary part variations, as reported in **Figure 7**. There is a change in the Nyquist plot due to gas interaction with the membrane. However, this change in the spectroscopy after the interaction with CO_2 cannot be regenerated. Hence EIS measurements cannot be used as the detection method of the gas sensor.

3.2.2. OCV Measurements

To evaluate the effectiveness of the chemical resistive CO_2 sensor, we focused on analyzing the membrane with the highest IL loading. We specifically selected the PIM1_Imp membrane, as it achieves the maximum possible IL content. This choice enabled us to thoroughly examine the sensor's ability to detect and respond to CO_2 using precise and controlled OCV measurements.

The graph presented in **Figure 8** depicts the impact of a 20 mL min^{-1} flow of CO_2 on the OCV, showcasing an approximate increase of 30 mV. Notably, this elevation can be entirely restored by employing a 100 mL min^{-1} flux of N_2. Furthermore, all the voltage fluctuation is attributable to the interaction between the

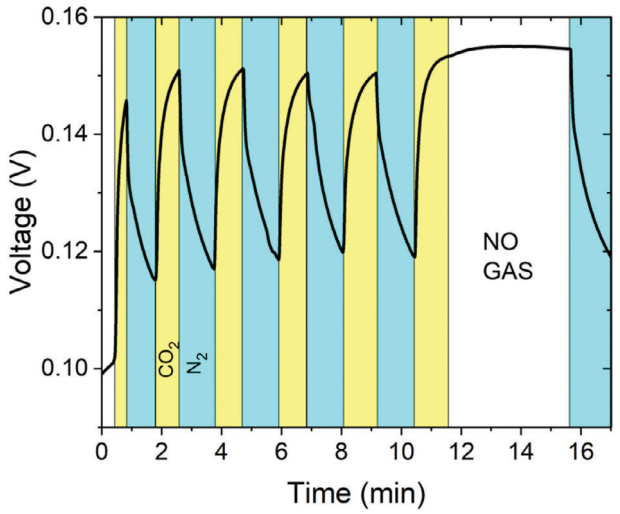

Figure 8. Repeatable voltage swing of the OCV during the alternate flushing of CO_2 and N_2 at 25 °C.

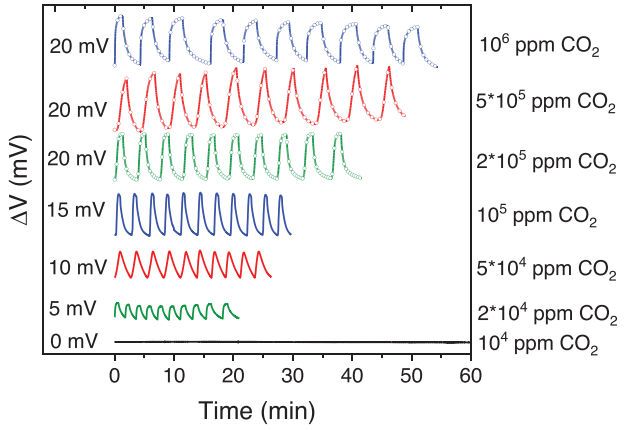

Figure 9. Repeated CO_2 adsorption/desorption tests at 25 °C.

sample and the gas stream. This assertion is supported by the fact that when the flow is halted (see minutes 12–16 on Figure 8), the OCV value is stable.

Following these preliminary assessments, we conducted a more comprehensive investigation into the membrane's long-term behavior under varying working conditions. Specifically, the focus was directed toward understanding the membrane's response over extended durations and exploring the implications of different CO_2 percentages within the gas flow. This detailed examination aimed to unravel the membrane's performance dynamics and elucidate the effects of varying CO_2 concentrations on its behavior.

3.2.3. OCV Measurements with CO_2/N_2 Mixture

For all CO_2 concentrations, a swing in voltage connected to the adsorption of CO_2 was obtained using a gas stream in OCV measurement. The procedure adopted consists in an adsorption of CO_2 for about 1 to 1.5 min under a total gas stream of 20 mL min^{-1} and then a regeneration under nitrogen at 150 mL min^{-1} until the voltage returns to the initial value.

For each gas mixture, the adsorption/desorption was performed for ten cycles.

As shown in **Figure 9**, it is possible to appreciate how the total voltage variation induced by the gas stream is dependent by the amount of CO_2 in the flow. Considering low CO_2 concentrations, it is possible to define an empirical detection limit of 2% of carbon dioxide, since this is the first concentration at which it is possible to observe an appreciable change in the OCV of the system. The voltage variation (ΔV) behaves in a logarithmic way with respect to the increase of CO_2 concentration, as shown in **Figure 10**. This behavior makes this sensor eligible for detecting the possible human toxicity of an environment. In the atmosphere, the percentage of CO_2 is ≈420 ppm (much lower than 1%),[32] while the percentage over which CO_2 becomes toxic for human body is 5%.[33] Thanks to the logarithmic dependance between $\%CO_2$ and ΔV, it is possible to evaluate when the carbon dioxide amount in a gas stream can becomes harmful for human health. To determine the sensitivity, this was evaluated by performing a linear fit of the experimental data. The equation which allows to fit the data in the best possible way is $\Delta V = 14.53*\log(\%CO_2) + 0.31$. Since

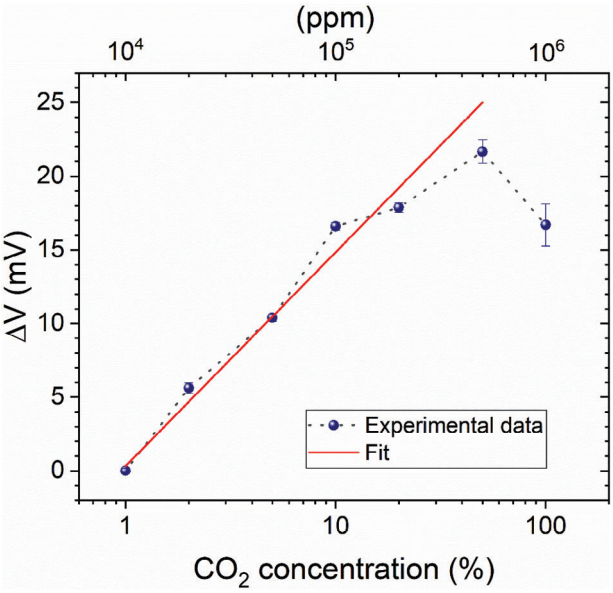

Figure 10. Induced voltage variation for different amount of CO_2 in the gas stream.

the sensitivity is defined as the angular coefficient of the just discussed curve, it is possible to define it as 14.53 mV $dec(\%CO_2)^{-1}$.

Long stability test were also performed as shown in **Table 3**. It is possible to appreciate how the membrane which undergoes the higher CO_2 concentration flux is also the one which reaches earlier the steady state, after ≈5 h. If we reduce gradually the concentration to 50% and 10%, the time required for steady state rises respectively up to 17 and 30 h. Moreover, considering the rising time of the membrane when it encounters CO_2 for the first time, this increases by reducing the concentration of CO_2 in the total flow. When reaching the lowest concentration of 1% of CO_2, the membrane does no longer reacts to the adsorption of CO_2.

The key parameters of our sensor and other sensors reported in the literature are listed and compared in **Table 4**. Compared with the listed studies, the CO_2 sensor developed in this work was easy to fabricate and had quite the widest range of detection ($2*10^4$–10^6 ppm). Most of the reported sensors were inflexible and worked at high temperatures. However, the sensor developed in this study is flexible and operates at room temperature.

Table 3. Response time on long exposure and maximum voltage variation induced during repeated adsorption/desorption test.

ppm CO_2	Response time (long exposure)	ΔV [mV] (repeated adsorption/desorption)
1.000.000[d]	1″	16.7
500.000[d]	1′26″	21.7
200.000[d]	1′48″	17.9
100.000[d]	15′	16.6
50.000[c]	10h	10.4
20.000[b]	25h	5.6
10.000[a]	ND	0

[a] 200 mL min^{-1}; [b] 100 mL min^{-1}; [c] 40 mL min^{-1}; [d] 20 mL min^{-1}.

Table 4. Sensor performance under different gas conditions (Adapted from Table 2 Rehman et al., 2023,[34] licensed under CC BY 4.0).

Sensing Material	Detection Range [ppm]	Response Time [s]	Recovery Time [s]	Operating Temperature[a] [°C]	Rev.	Flex.
This work	$2*10^4$–10^6	90		25	Yes	Yes
p(D-co-M)[34]	10^4–10^6	360	840	RT	Yes	Yes
PEI- CNTs[35]	200–1000	600	600	RT	Yes	Yes
PEDOT/PSS, graphene[36]	400–4200	NA	NA	50 and 60	No	Yes
ZnO nanoflakes[37]	200–1025	9–17	9–17	250	Yes	Yes
PEI-PANI[38]	50–5000	440 ± 313	601 ± 292	RT	Yes	No
SPES/e-MWCNTs[39]	500–5000	480–840	1620	RT	Yes	No
PES/e-MWCNTs[39]	500–5000	600–960	1620	RT	Yes	No
PEI/PEG[40]	200–$25*10^4$	251	300	RT	Yes	No
Y-HEC[41]	250–10^4	49–190	80–200	RT	Yes	No
SPEEK-5/d-MWCNTs[42]	500–5000	250–665	1322–1622	RT	Yes	No
Ni-SnO_2[43]	0–200	4	13	275	Yes	No
Yolk-shell CeO_2 nanospheres[44]	150–2400	154.8	245	100	Yes	No
ZnO thin films[45]	50–1000	100–300	100–400	300–450	Yes	No
GO/CuO_X nanocomposite[46]	250–750	25	8	100	Yes	No
N-doped ZnO[47]	100–5000	NA	NA	250	Yes	No
CNT-PEI-PEG[48]	400–2000	1200	1200	22–26	Yes	No
$La_2O_2CO_3$[49]	0–4000	NA	NA	20	Yes	No
SnO_2 nanoparticles[50]	50–1000	480–660	480–600	250–350	Yes	NA
NiO-doped SnO_2 thin films[51]	500–10^4	13	34	50	Yes	NA
GA@UiO-66-NH_2[52]	$5*10^4$–10^6	18	18	200	Yes	No
p-Si/MoO_3[53]	50–150	14–18	8–20	150–250	Yes	No

[a] RT means room temperature.

Furthermore, the sensor was reversible with a response time of 90 s. Altogether, the fabricated sensor offered superior features that overcome the challenges that exist in current CO_2 sensing devices.

4. Conclusion

This study successfully presents the development and evaluation of a novel potentiometric CO_2 sensor using PIM-1 membranes impregnated with [DBUH][Im]. The integration of the microporous structure of PIM-1 and the high CO_2 absorption capacity of the imidazolate-based ionic liquid has resulted in a highly effective sensor with enhanced sensitivity and selectivity for carbon dioxide detection. The results demonstrate the significant potential of this material combination for various gas sensing applications.

The PIM-1/DBU imidazolate membranes have proven to be robust and stable, effectively preventing ionic liquid leakage, which is a common challenge in traditional gas sensors. This stability, coupled with the high efficiency in CO_2 capture and release, highlights the suitability of these membranes for long-term use in environmental and industrial monitoring. The TGA and FTIR analyses confirmed that the membranes maintain their structural integrity and functional performance over extended periods, even under varying CO_2 concentrations.

Moreover, the versatility of the PIM-1/DBU imidazolate membranes extends their applicability to a wide range of scenarios, including air quality control and industrial process monitoring. The sensors demonstrated an impressive ability to detect CO_2 at different concentrations, showcasing their potential to contribute significantly to environmental sustainability and safety. The ability to absorb and desorb CO_2 efficiently makes these membranes ideal for real-time monitoring applications where rapid response and high sensitivity are critical.

The study opens promising avenues for future research, suggesting that further exploration into other types of ionic liquids or polymers could enhance the selectivity and sensitivity of gas sensors for different target gases paving the way for the development of a new generation of advanced, sustainable, and efficient gas sensors tailored to meet specific needs in various sectors.

In conclusion, the PIM-1/[DBUH][Im] membranes represent a major advancement in the field of gas sensing technology. They offer a practical and effective solution for CO_2 detection, significantly contributing to the development of sustainable materials and technologies for environmental monitoring. The findings of this research provide a solid foundation for the future development of innovative gas sensors, underscoring the importance of polymer-ionic liquid composites in advancing gas sensing capabilities and addressing critical environmental challenges.

Acknowledgements

This article was partially funded under the National Recovery and Resilience Plan (NRRP), Mission 4 "Education and Research"—Component

2 "From research to business"—Investment 3.1 "Fund for the realization of an integrated system of research and innovation infrastructures"—Call for tender No. n. 3264 of 28/12/2021 of Italian Ministry of Research funded by the European Union—NextGenerationEU—Project code: IR0000027, Concession Decree No. 128 of 21/06/2022 adopted by the Italian Ministry of Research, CUP: B33C22000710006, Project title: iENTRANCE. This study was carried out within the Agritech National Research Center and received funding from the European Union Next-GenerationEU (PIANO NAZIONALE DI RIPRESA E RESILIENZA (PNRR) – MISSIONE 4 COMPONENTE 2, INVESTIMENTO 1.4 – D.D. 1032 June 17, 2022, CN00000022). Furthermore, authors wish to thank European Union for the financial support through the Next Generation EU- projects "Nord Ovest Digitale E Sostenibile-NODES" (PNRR, D.D. n.1054 June 23, 2022), the NEST "Network for Energy Sustainable Transition- NEST"(PE0000021, D.D. n.341 March 15, 2022). Authors also acknowledge Ministero dello Sviluppo Economico (MISE) and Ministero della Transizione Ecologica (MITE) for the financial support. These results were part of a project that had received funding from the European Research Council (ERC) under the European Union's ERC Starting Grant agreement "CO2CAP" No. 949916. This manuscript reflects only the authors' views and opinions, neither the European Union nor the European Commission can be considered responsible for them.

Conflict of Interest

The authors declare no conflict of interest.

Data Availability Statement

The data that support the findings of this study are available from the corresponding author upon reasonable request.

Keywords

electrochemical impedance spectroscopy, gas sensing, ionic conductivity, ionic liquids, polymer of intrinsic microporosity

Received: June 10, 2024
Revised: August 12, 2024
Published online:

[1] M. W. Jones, G. P. Peters, T. Gasser, R. M. Andrew, C. Schwingshackl, J. Gütschow, R. A. Houghton, P. Friedlingstein, J. Pongratz, C. Le Quéré, *Sci. Data* **2023**, *10*, 155.
[2] Health and Safety Executive, EH40/2005 Workplace Exposure Limits: Containing the List of Workplace Exposure Limits for Use with the Control of Substances Hazardous to Health Regulations 2002 (as Amended), 4th ed., The Stationery Office, London **2020**, pp. 1–74.
[3] L. Chatzidiakou, D. Mumovic, A. J. Summerfield, *Intell. Build. Int.* **2012**, *4*, 228.
[4] J. Prakash, P. R. de Oliveira, H. C. Swart, M. Rumyantseva, M. Packirisamy, B. C. Janegitz, X. Li, *Sens. Diagn.* **2022**, *1*, 1143.
[5] S. D. Lawaniya, S. Kumar, Y. Yu, H.-G. Rubahn, Y. K. Mishra, K. Awasthi, *Mater. Today Chem.* **2023**, *29*, 101428.
[6] H. Yuan, J. Tao, N. Li, A. Karmakar, C. Tang, H. Cai, S. J. Pennycook, N. Singh, D. Zhao, *Ang. Chem. Int. Edi.* **2019**, *58*, 14089.
[7] G. Hanrahan, D. G. Patil, J. Wang, *J. Environ. Monit.* **2004**, *6*, 657.
[8] B. J. Privett, J. H. Shin, M. H. Schoenfisch, *Anal. Chem.* **2008**, *80*, 4499.
[9] F. D. Mainuddin, U. Mittal, J. Kumar, A. T. Nimal, *IETE Tech. Rev.* **2021**, *38*, 611.
[10] J. Devkota, D. W. Greve, T. Hong, K.-J. Kim, P. R. Ohodnicki, *IEEE Sens. J.* **2020**, *20*, 9740.
[11] G. Joshi, J. K. Rajput, L. P. Purohit, *Microporous Mesoporous Mater.* **2021**, *326*, 111343.
[12] C. A. Zito, T. M. Perfecto, A.-C. Dippel, D. P. Volanti, D. Koziej, *ACS Appl. Mater. Interfaces* **2020**, *12*, 17745.
[13] K.-C. Hsu, T.-H. Fang, Y.-J. Hsiao, C.-A. Chan, *Mater. Lett.* **2020**, *261*, 127144.
[14] L. Lan, J. Chen, X. Zhao, H. Ghasemifard, *IEEE Sens. J.* **2019**, *19*, 4923.
[15] Y. Liu, H. Lin, B. A. Z. Montano, W. Zhu, Y. Zhong, R. Kan, B. Yuan, J. Yu, M. Shao, H. Zheng, *Photoacoustics* **2022**, *25*, 100332.
[16] M. Gupta, H. F. Hawari, P. Kumar, Z. A. Burhanudin, *Crystals* **2022**, *12*, 264.
[17] E. S. Muckley, T. Aytug, R. Mayes, A. R. Lupini, J.-M. Y. Carrillo, M. Goswami, B. G. Sumpter, I. N. Ivanov, *ACS Appl. Mater. Interfaces* **2019**, *11*, 48466.
[18] H. Wang, D. Chen, M. Zhang, J. Wang, *Surf. Coat. Technol.* **2017**, *320*, 542.
[19] H. Wang, H. Chen, M. Zhang, J. Wang, J. Sun, *Ionics* **2019**, *25*, 3397.
[20] S. Bouachma, K. Ayouz-Chebout, M. Kechouane, A. Manseri, C. Yaddadene, H. Menari, N. Gabouze, *Appl. Phys. A* **2021**, *128*, 69.
[21] E. W. Graef, B. Jagannath, R. Munje, S. Prasad, *IEEE Sens. J.* **2018**, *18*, 3517.
[22] C. Zhang, K. Xu, K. Liu, J. Xu, Z. Zheng, *Coord. Chem. Rev.* **2022**, *472*, 214758.
[23] P. Kassal, M. D. Steinberg, I. M. Steinberg, *Sens. Actuators, B* **2018**, *266*, 228.
[24] M. Taheri, M. Ketabi, A. M. Al Shboul, S. Mahinnezhad, R. Izquierdo, M. J. Deen, *ACS Omega* **2023**, *8*, 46794.
[25] R. S. Andre, R. C. Sanfelice, A. Pavinatto, L. H. C. Mattoso, D. S. Correa, *Mater. Des.* **2018**, *156*, 154.
[26] M. W. Shinwari, D. Zhitomirsky, I. A. Deen, P. R. Selvaganapathy, M. J. Deen, D. Landheer, *Sensors* **2010**, *10*, 1679.
[27] R. S. Andre, R. C. Sanfelice, A. Pavinatto, L. H. C. Mattoso, D. S. Correa, *Membranes* **2022**, *12*, 1262.
[28] G. Ferraro, C. Astorino, M. Bartoli, A. Martis, S. Lettieri, C. F. Pirri, S. Bocchini, *Membranes* **2022**, *12*, 1262.
[29] Y. Zhang, Z. Wu, S. Chen, P. Yu, Y. Luo, *Ind. Eng. Chem. Res.* **2013**, *52*, 6069.
[30] E. Davarpanah, S. Hernández, G. Latini, C. F. Pirri, S. Bocchini, *Adv. Sustainable Syst.* **2019**, *4*, 1900067.
[31] G. Latini, M. Signorile, V. Crocellà, S. Bocchini, C. F. Pirri, S. Bordiga, *Catal. Today* **2019**, *336*, 148.
[32] NOAA Research, "Coronavirus response barely slows rising carbon dioxide", https://research.noaa.gov/2021/06/07/coronavirus-response-barely-slows-rising-carbon-dioxide/, (accessed: June **2024**).
[33] a) K. Permentier, S. Vercammen, S. Soetaert, C. Schellemans, *Int. J. Emerg. Med.* **2017**, *10*, 142; b) Centers for Disease Control and Prevention, "IDLH Documentation: Carbon Dioxide", https://www.cdc.gov/niosh/idlh/124389.html, (accessed: June **2024**).
[34] Z. Shahrbabaki, S. Farajikhah, M. B. Ghasemian, F. Oveissi, R. J. Rath, J. Yun, F. Dehghani, S. Naficy, *Adv. Mater. Technol.* **2023**, *8*, 2201510.
[35] M. Han, S. Jung, Y. Lee, D. Jung, S. H. Kong, *Micromachines* **2021**, *12*, 1053.
[36] B. Andò, S. Baglio, G. Di Pasquale, A. Pollicino, S. Graziani, C. Gugliuzzo, C. Lombardo, V. Marletta, *Energies* **2019**, *12*, 557.
[37] S. Kanaparthi, S. G. Singh, A. C. S. Appl, *Nano Mater.* **2019**, *2*, 1496.
[38] S. Srinives, T. Sarkar, R. Hernandez, A. Mulchandani, *Anal. Chim. Acta* **2015**, *874*, 40.
[39] S. Bag, K. Pal, *IEEE Trans. Nanotechnol.* **2019**, *18*, 1119.
[40] L. Liu, S. Sang, D. Han, Z. Liu, X. Han, D. Li, Y. Chen, D. Liu, X. Liu, K. Yang, *Sens. Actuators, B* **2022**, *369*, 132303.

[41] V. R. Naganaboina, M. Anandkumar, A. S. Deshpande, S. G. Singh, A. C. S. Appl, *Nano Mater.* **2022**, *5*, 4524.
[42] S. Bag, K. Pal, *Sens. Actuators* **2020**, *303*, 127115.
[43] V. Manikandan, I. Petrila, S. Vigneselvan, R. Mane, B. Vasile, R. Dharmavarapu, S. Lundgaard, S. Juodkazis, J. Chandrasekaran, *RSC Adv.* **2020**, *10*, 3796.
[44] C. A. Zito, T. M. Perfecto, A.-C. Dippel, D. P. Volanti, D. Koziej, *ACS Appl. Mater. Interfaces* **2020**, *12*, 17745.
[45] T. Karthik, A. Hernández, Y. Kudriavtsev, H. Gómez-Pozos, M. Ramírez-Cruz, L. Martínez-Ayala, A. Escobosa-Echvarria, *J. Mater. Sci.: Mater. Electron.* **2020**, *31*, 7470.
[46] S. Keerthana, K. Rathnakannan, *J. Mater. Sci.: Mater. Electron.* **2021**, *32*, 23513.
[47] Y. Xia, A. Pan, Y.-Q. Su, S. Zhao, Z. Li, A. K. Davey, L. Zhao, R. Maboudian, C. Carraro, *Sens. Actuators, B* **2022**, *357*, 131359.
[48] Z. A. Siefker, A. Boyina, J. E. Braun, X. Zhao, B. W. Boudouris, N. Bajaj, G. T.-C. Chiu, J. F. Rhoads, *IEEE Sensors*, IEEE, Piscataway, NJ **2020**.
[49] T. Suzuki, A. Sackmann, A. Oprea, U. Weimar, N. Bârsan, *ACS Sens.* **2020**, *5*, 2555.
[50] C. Chaitra, H. Kalpana, C. Ananda, H. Lalithamba, *Mater. Technol.* **2022**, *37*, 2339.
[51] J. M. Rzaij, N. F. Habubi, *J. Mater. Sci.: Mater. Electron.* **2022**, *33*, 11851.
[52] K. Jayaramulu, M. E. DMello, K. Kesavan, A. Schneemann, M. Otyepka, S. Kment, C. Narayana, S. B. Kalidindi, R. S. Varma, R. Zboril, *J. Mater. Chem. A* **2021**, *9*, 17434.
[53] T. Thomas, Y. Kumar, J. A. R. Ramón, V. Agarwal, S. S. Guzmán, R. Reshmi, S. Pushpan, S. L. Loredo, K. Sanal, *Vacuum* **2021**, *184*, 109983.